Computers & Graphics (2021)

Contents lists available at ScienceDirect

Computers & Graphics

journal homepage: www.elsevier.com/locate/cag

An Improved Refinement Rule for Multi-sided Faces

Kęstutis Karčiauskas and Jörg Peters*

ARTICLE INFO

Article history:
Received November 7, 2021

Keywords: mesh refinement, multi-sided faces, subdivision, free-form surface, shape, highlight lines, T-gon

ABSTRACT

Multi-sided faces arise in polyhedral modeling through introduction of features not aligned with the regular grid structure, e.g. when trimming off corners or merging primary shapes. A standard first step is to split the n-gon into n quadrilaterals that join at the n-gon's centroid. A canonical example is the 'face point rule' of Catmull-Clark subdivision.

We show that centroid-split rules negatively impact shape – already in the single, first refinement step. A new alternative face (and edge) rule improves the shape of surfaces controlled by the refined mesh noticeably. The improved face rule has a moderately increased footprint compared to the Catmull-Clark rule but remains simple in that it is characterized by just one scalar weight for each n.

1. Introduction

For $n \neq 4$, the n-sided face refinement rule of the Catmull-Clark algorithm [1] appears to have little importance since it applies only once: after the first refinement step all faces are 4-sided, as in Fig. 1 b. However, this first step determines macroscopic shape and influences the uniformity of the highlight line distribution [2] on the surface. Regardless of what algorithm is selected *afterwards* to turn the once-refined mesh into a surface, e.g. Catmull-Clark subdivision to the limit, curvature-bounded subdivision or some high-end polynomial surface construction, the resulting surface shows more visible large-scale artifacts and oscillations in the highlight lines when the first classical Catmull-Clark step (called *FEV* hereafter, for face, edge and vertex rule, respectively (F), (E), (V)) is replaced by a new improved step *FEV**.

In the broader context, analysis of recursive refinement or subdivision of polyhedral models has traditionally focused on the limit surface (see e.g. [3]). By contrast, this paper focusses on shape problems that arise from the *first* refinement step, when an n-sided face of the polyhedral model is split into quads by joining points near the mid-edges to the centroid average of

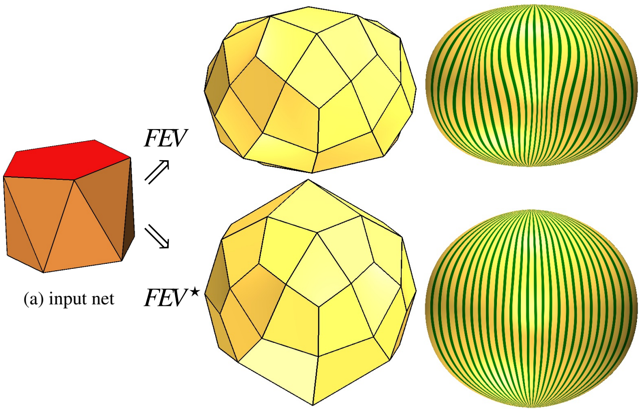

(a) input net (b) 1st step (c) surface completion

Fig. 1: One refinement step of multi-sided faces followed by Catmull-Clark subdivision to the limit. *top*: *FEV* = first step of Catmull-Clark refinement. *bottom*: *FEV** = first step of the new improved refinement. The new face-point rule reduces flatness and oscillations.

---

*Corresponding author: jorg.peters@gmail.com

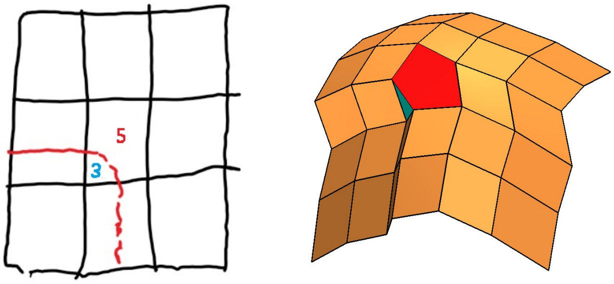

(a) sketch (b) input with feature

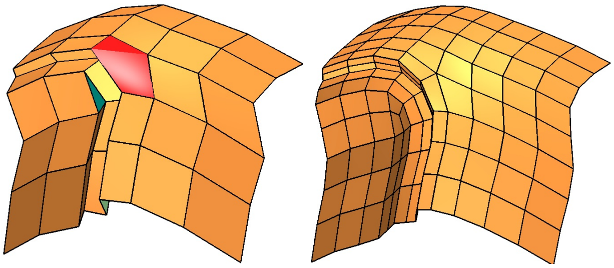

(c) groove inserted (d) 1× refined mesh

Fig. 2: (a) Initial sketch with feature line splitting a quad face into a 3-sided and a 5-sided face. (b) Input mesh. (c) Insertion of a groove. (d) One refinement step.

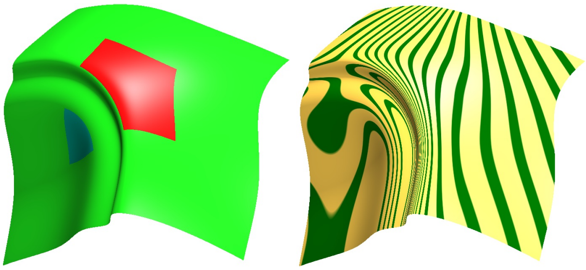

(a) surface layout and highlight lines of *FEV** + [4]

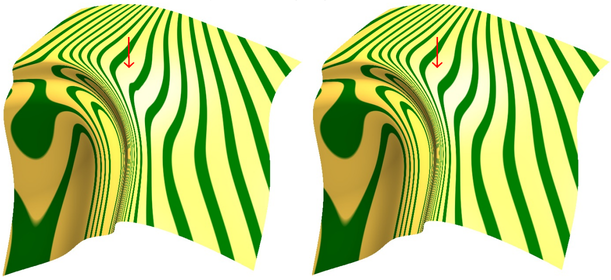

(b) *FEV* + [1] (c) *FEV* + [4]

Fig. 3: Example Fig. 2 continued. (a) *left*: bi-3 patches, and surface completion of 3- and 5-sided regions according to [4]. (b,c) shows flatness and higher oscillations in the highlight lines (see [2]) due to *FEV* rather than *FEV**. The kink in the highlight lines (see ↓) when applying [1] is reduced to a wave in (c) by creating the surface with [4]. The highlight line distribution is far more uniform in (a), when applying the improved first step rule *FEV**.

the n-gon's corners. This split ensures that all faces are quadrilaterals. Quad meshes can serve as control nets of a number of existing surface constructions for multi-sided surface pieces. Yet, even when a high-quality construction is applied after one Catmull-Clark step, the resulting surfaces suffer from oscillating highlight lines and unwanted flatness as demonstrated in Fig. 1 c, top.

Multi-sided faces arise in polyhedral, control net based modeling in several situations. Polyhedral designs typically progress in a hierarchical fashion as illustrated in Fig. 2 : Starting with a sketch (a), a feature line splits the center face (b) into a 3-sided and a 5-sided face. In (c) the feature line is emphasized by inserting two quad strips to form a groove. A single refinement step yields a mesh (d) consisting entirely of quads. The resulting mesh is used as a control net for subdivision Fig. 3 b or other multi-sided surface algorithms Fig. 3 a,c. Based on rule *FEV*, Fig. 3 b and c show higher oscillations and a wider spread of highlight lines in the area of the 5-sided facet when compared to surfaces based on *FEV**, see Fig. 3 a. The wider spread indicates flatness. The combination *FEV**+[1] has a uniform highlight line distribution with high-frequency oscillations due to the eigenstructure of [1]. (This behavior is not shown here but in detail in Fig. 16 and Fig. 18 .)

Multi-sided faces also arise in re-meshing, e.g. [5, 6, 7, 8, 9]. For example, the layout in Fig. 2 b can equally result from two T-junctions on one quadrilateral in a quad-dominant layout: connecting the T-junctions yields a pair of a 3-sided and a 5-sided configuration. So the new rule can serve as the 'poor man's' alternative to the specialized treatment of T-junctions via algorithms such as [10, 11, 12].

The contributions of this paper are

- an improved refinement rule *FEV** for meshes with multi-sided faces. The rule *FEV** is characterized by a single scalar weight μ_n, see Fig. 4 d and (2).
- The rule is based on the unusual approach of inverting the Catmull-Clark limit formula.
- Numerous examples (Section 4) show that, compared to one step of the Catmull-Clark face rule (*FEV*), the new rule (*FEV**) improves the shape for subsequent surface constructions.

We will illustrate the last point with four algorithms for constructing multi-sided surface caps: two subdivision algorithms and two constructions based on geometric continuity.

Overview: After the literature review in Section 1.1, Section 2 introduces the improved rule. The rule is easy to implement. Section 3 derives the improved rule, *FEV**. A reader focused on application can skip this theory contribution. Section 4 presents examples and explains choices by looking at: Section 4.1 surfaces from a simple polyhedral input net with one multi-sided face; Section 4.2 surfaces from nets with T-junctions; and Section 4.3 surfaces from nets with many, including tightly-packed irregularities.

1.1. Literature

Catmull-Clark subdivision rules [1] generalize the refinement, induced by uniform knot-insertion into uniform bi-cubic (bi-3) tensor-product splines, to polyhedral control nets with n-valent vertices and m-sided faces. As is well-known, repeated Catmull-Clark subdivision steps [1] accumulate hyperbolic terms resulting in geometric artifacts near so-called extraordinary points, namely the limit of mesh nodes of valence $n > 4$. When $n > 4$, [13] showed that even for convex input meshes the limit surfaces of Catmull-Clark subdivision are hyperbolic at extraordinary points. A number of algorithms, with

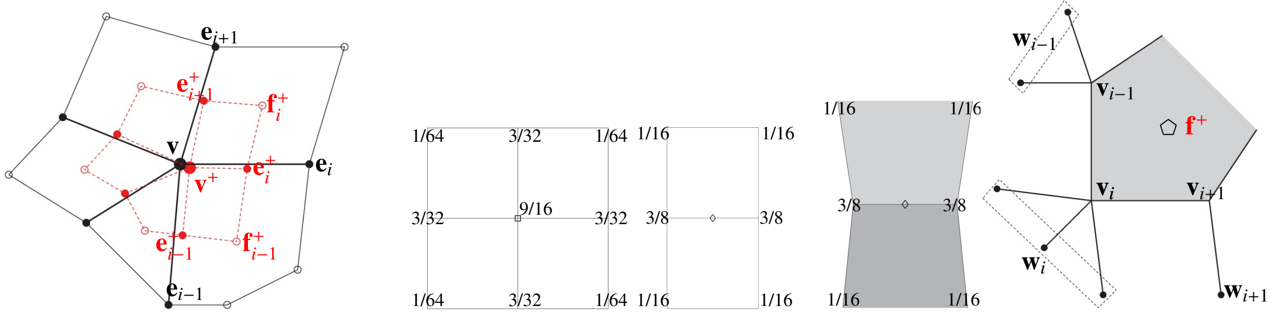

(a) refinement pattern (b) regular stencils (c) E_2 stencil (d) Improved face point rule $F^\star$

Fig. 4: Refinement rules. (a) General structure of a midpoint split. The input vertices are black, the new vertices are red. (b) Regular vertex rule for □ and edge rule for ⋄. (c) Generalized edge point for ⋄ with multi-sided shaded areas. (d) Improved rule (1) for the new face point: $\mathbf{f}^+_i := \mu_n\overline{\mathbf{v}} + (1-\mu_n)\overline{\mathbf{w}}$ with weights μ_n, $\mathbf{w}_i$ = average of the direct neighbors of $\mathbf{v}_i$ not on the multi-sided face; and $\overline{\mathbf{w}} := \sum_{j=0}^{n-1}\mathbf{w}_j/n$, $\overline{\mathbf{v}} := \sum_{j=0}^{n-1}\mathbf{v}_j/n$.

increased complexity, have been devised to remedy this flaw in the limit, see e.g. [14, 15, 16, 17]. For example, tuning subdivision weights [15, 16] addresses this deficiency by adjusting the differential expansion at the extraordinary point. [17] directly prescribes leading parts of the eigenstructure. Guided Subdivision [14] removes artifacts by prescribing the limit differential expansion directly and geometrically by a guide surface that yields the wanted eigenstructure. In all cases, this comes at the cost of more complex rules to generate the contracting subdivision surface rings. And, as the table of surfaces resulting from 'truncated cone' input nets, Fig. 10 , amply illustrates, for at least one of the algorithms, [16], such improvement come at the cost of other high-frequency artifacts. The new rule improves the low frequency shape of all such subdivision surfaces.

[18] notes that 'It may be necessary to focus on one artifact at the early stage and on others at later stages.' Indeed artifacts at the center, like divergent curvatures and forced hyperbolic shape, warrant adjustment of the eigenstructure of the subdivision matrix, whereas artifacts like repeated kinks and pinching highlight lines show up most strongly for the early sequence of subdivision surface rings. For regular control nets, [19] highlights the importance of the (box-) spline averaging directions. In particular, the first subdivision steps have large scale, visible influence so that large scale features better be aligned with the preferred subdivision directions to avoid artifacts. The astute focus of many of Malcolm Sabin's presentations that there are 'first step artifacts' motivates the new rule of this paper. For the irregular nets of this paper, too small a footprint that ignores the secondary neighborhood for the first step refinement rules leads to undue flatness and oscillation.

Another way to evaluate the new improved rule is to observe that by joining points near the mid-edges to the centroid average of the n-gon's corners all faces become quadrilaterals and so enable piecewise tensor-product spline surface constructions. For example, [20, 4, 21] generalize bi-cubic spline surfaces where $n \neq 4$ quads join. Alternatively, [21] is a hybrid construction that generates guided subdivision rings completed by a tiny central cap to support hierarchical design or refinement for engineering analysis, see Fig. 16 . The impact of the new rule on shape can therefore be assessed by applying piecewise polynomial high-end surface constructions to the refined control net.

Non-polynomial constructions based on transfinite interpolation [22, 23, 24, 25] or Gregory patches [26] for multi-sided regions are only indirectly related to the challenge considered in this paper, in that, there too, internal face control points have to be chosen carefully to avoid shape artifacts.

2. Improved rules for meshes with multi-sided faces

The classic Catmull-Clark refinement rules [1, 27] call a node of the once-refined control net a 'new point', see Fig. 4a . We label the rules as (F) (E_1) and (V), and their one-time application as *FEV*:

- ▹ (F) A new face point $\mathbf{f}^+_i$ is the average of all vertices of the facet with corners $\mathbf{e}_i$, $\mathbf{v}$, $\mathbf{e}_{i+1}$.
- ▹ (E_1) A new edge point is set as $\mathbf{e}^+_i := \frac{1}{4}(\mathbf{v}+\mathbf{e}_i+\mathbf{f}^+_{i-1}+\mathbf{f}^+_i)$.
- ▹ (V) A new vertex point is defined by

$$\mathbf{v}^+ := \frac{n-2}{n}\mathbf{v} + \frac{\overline{\mathbf{e}} + \overline{\mathbf{f}^+}}{n}, \quad \overline{\mathbf{e}} := \frac{1}{n}\sum_{i=0}^{n-1}\mathbf{e}_i, \quad \overline{\mathbf{f}^+} := \frac{1}{n}\sum_{i=0}^{n-1}\mathbf{f}^+_i.$$

For abutting quads, (E_1) has the stencil in Fig. 4 b,*right*. Applying this stencil to facets that are not quads, see Fig. 4 c, by choosing the points closest to the common edge and the same point twice in the case of a triangle, yields an alternative rule (E_2). Section 3 derives the following new rules whose one-time application defines one step *FEV**:

- ($F^\star$) The improved face point rule for the n-sided face with corners $\mathbf{v}_i$, $i = 0, \dots, n-1$ is (see Fig. 4d):

$$\mathbf{f}^+ := \mu_n \overline{\mathbf{v}} + (1-\mu_n)\overline{\mathbf{w}}, \tag{1}$$

$$\overline{\mathbf{v}} := \sum_{j=0}^{n-1} \mathbf{v}_j/n, \quad \overline{\mathbf{w}} := \sum_{j=0}^{n-1} \mathbf{w}_j/n$$

  where $\mathbf{w}_i$ is the average of direct neighbor nodes of $\mathbf{v}_i$ (enclosed by dashed boxes in Fig. 4 d) that are not on the multi-sided face; and

$$\mu_n := \begin{cases} \frac{7}{8}, & n = 3, \\ 1, & n = 4, \\ \frac{2.64309n - 0.45291n^2}{1+1.94025n-0.36163n^2}, & n > 4. \end{cases} \tag{2}$$

- ($E^\star$) The improved edge point rule averages (E_1) and (E_2) with equal weight $\frac{1}{2}$. Note that (E_1) uses the improved face points $\mathbf{f}^+_{i-1}$ and $\mathbf{f}^+_i$.
- ($V^\star$) The improved vertex rule applies (V) with improved edge points and points $\mathbf{f}^+_i$.

For a quad face, since $\mu_4 := 1$, $\mathbf{f}^+_i$ is the average of the quad's vertices, i.e. corresponds to standard spline knot insertion.

Since all faces created by the first refinement are 4-sided, after the first step only classic rules apply. Although the macroscopic shape is altered, the characterization of the limit smoothness of a subsequent subdivision algorithm is therefore unaffected by the improved first step: the limit behaviour of any subsequent subdivision algorithm at its extraordinary point is the limit behavoir of the subdivision algorithm.

3. Derivation of the improved rules

The new rules are motivated by four observations. First, the existing theory does not provide a good choice of *new central node* (that split an n-sided control net face) for meshes with multi-sided faces. In particular, applying *FEV* to convex configurations yields unduly flat surfaces. Second (except when $n = 3$, see [4]) Catmull-Clark limit points of n-valent nodes perform well as the *central points* where n surface patches meet in high-quality surface constructions such as [20, 4, 21]. Third, setting the central surface point by optimizing a linear functional over a *small* number of degrees of freedom reduces oscillations or flatness compared to approaches optimizing over many free parameters. Fourth, surface quality is a partly subjective and application-dependent notion. The quality of an algorithm is currently measured as the absence of flat regions or visible oscillations in the highlight line distribution [2] of surfaces generated by the algorithm on an obstacle course of input control nets.

The following approach addresses and leverages the four observations: we symbolically fit a construction with few degrees of freedom and use the Catmull-Clark limit point as central point ⊙ to deduce a formula for a central control node $\mathbf{f}^+$ for the refinement *FEV**. The rule is optimized to reduce flatness and highlight line oscillations as tested by applying a number of surface constructions to the refined net.

The derivation in the following subsections starts with a polyhedral net where an n-sided face is surrounded by two layers of quadrilaterals, see Fig. 6 a. We first determine a symbolic expression for the central point ⊙ of a surface cap. Since the once-refined net has the structure of a CC-net shown in Fig. 5 b, we can then invert the Catmull-Clark formula for limit points to obtain formula for the n-valent control node $\mathbf{f}^+$ in terms of the central point. Due to the fourth observation above, some steps of the derivation are justified by the extensive experiments sketched in Section 4. The following four subsections explain the technical details of the derivation.

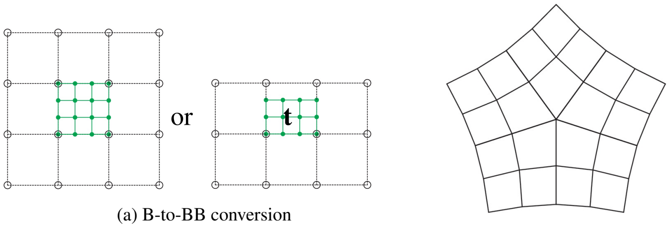

(a) B-to-BB conversion

(b) CC-net

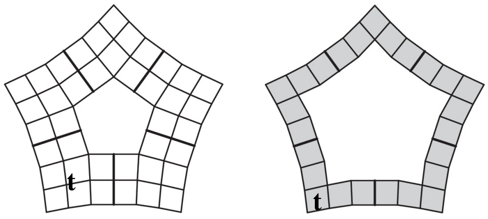

(c) **t** of order 2

(d) **t** of order 1

Fig. 5: Control nets and Bernstein-Bézier coefficients. (a) B-spline-to-Bernstein-Bézier net conversion (*left*) complete conversion, (*right*) partial conversion to form **t**. (b) A generalized B-spline-like CC-net: an extraordinary (central) node of valence $n = 5$ surrounded by two layers of quads. The nodes of the first layer are regular, that is, of valence 4. (c) Tensor-border **t** of order 2 defined from the CC-net B-to-BB conversion. (d) A first-order tensor-border **t** defines positions and first derivatives across each edge of the n *L*-shaped pieces.

3.1. *From B-spline to BB-form and tensor-borders* t

We represent surfaces as piecewise tensor-product patches of bi-degree d (short bi-d) in Bernstein-Bézier form (BB-form), see e.g. [28]:

$$\mathbf{b}(u,v) := \sum_{k=0}^{d}\sum_{\ell=0}^{d} \mathbf{b}_{k\ell} B_k^d(u) B_\ell^d(v), \quad 0 \le u, v \le 1.$$

Here $B_i^d(t) := \binom{d}{i}(1-t)^{d-i}t^i$ are the Bernstein polynomials of degree d and $\mathbf{b}_{ij}$ are the BB-coefficients. Connecting $\mathbf{b}_{ij}$ to $\mathbf{b}_{i+1,j}$ and $\mathbf{b}_{i,j+1}$ wherever possible yields the *BB-net*. Any 4×4 sub-grid with control points marked ∘ in Fig. 5 a,*left* can be interpreted as the control points of a uniform bi-3 B-spline. *B-to-BB conversion* expresses the spline in bi-3 BB-form as illustrated by the green BB-net. Conversion of a partial sub-grid yields a partial BB-net, see Fig. 5 a,*right* called a *tensor-border*. The tensor-border of order 2, denoted **t**, defines a position, the first and second derivatives across an edge. To double the scale of first-order Hermite data at $\tilde{\mathbf{b}}_{00} := \mathbf{b}_{00}$, the initial BB-coefficients $\mathbf{b}_{ij}$, $0 \le i, j \le 1$ are transformed to

$$\begin{aligned} \tilde{\mathbf{b}}_{10} &:= 2\mathbf{b}_{10} - \mathbf{b}_{00}, \quad \tilde{\mathbf{b}}_{01} := 2\mathbf{b}_{01} - \mathbf{b}_{00}, \\ \tilde{\mathbf{b}}_{11} &:= 4\mathbf{b}_{11} - 2\mathbf{b}_{10} - 2\mathbf{b}_{01} + \mathbf{b}_{00}. \end{aligned} \tag{3}$$

3.2. Determining the central point $\odot$

We adapt to our setting a construction that was used as an intermediary step in (Sect 4 of) [29].

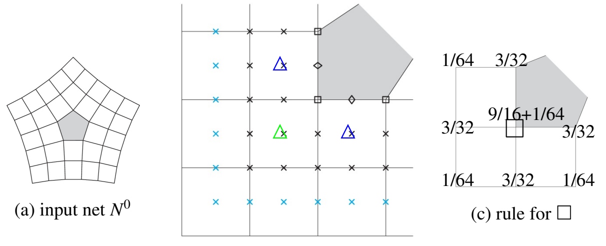

(a) input net N^0

(b) refined net N^1

(c) rule for □

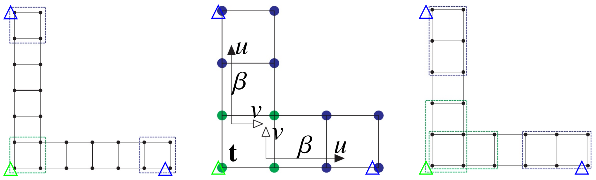

(d) B-to-BB

(e) bi-3 **t**

(f) bi-5 $\mathbf{t} \circ \beta$

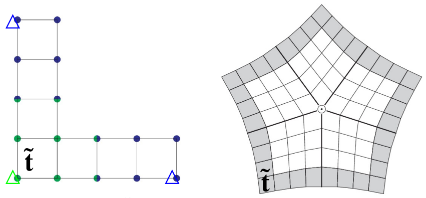

(g) bi-4 $\tilde{\mathbf{t}}$

(h) bi-4 cap

Fig. 6: Derivation of the central point $\odot$ in (h); the anchors △ and △ aid orientation.

Fig. 6 illustrates the derivation of the central point $\odot$ on the surface. The input net N^0 is an n-sided face (marked gray in Fig. 6 a and thereafter) surrounded by two layers of quads so that all interior vertices are regular, i.e. have valence 4. Fig. 6 b displays one sector of the refined net N^1. Nodes onf N^1 marked $\diamond$ stem from the (E_2) edge rule, nodes marked □ by the special vertex rule of Fig. 6 c, and nodes marked $\times$ by uniform knot insertion ('regular' rules). The outermost layer of $\times$ is not needed for the derivation.

Fig. 6 d shows a tensor-border of order 1 obtained from N^1 by partial B-to-BB conversion. Applying (3) at the locations marked by the 'anchors' △ and △, and merging the resulting 2×2 BB-nets yields the order 1 bi-3 tensor-border **t**, shown in Fig. 6 e. Reparameterizing **t** along each edge with

$$\beta(u,v) := [u, a(u)v], \quad \mathsf{c} := \cos\frac{2\pi}{n}, \tag{4}$$
$$a(u) := B_0^2(u) + B_1^2(u) + \frac{2}{2-\mathsf{c}}B_2^2(u),$$

yields $\mathbf{t} \circ \beta$ of degree bi-5, in Fig. 6 f (and corrects a typo in [29]). The 3×2 arrangements enclosed by dashed rectangles in Fig. 6 f are re-expressed in bi-4 form and merged, averaging at the shared, overlapping locations. This yields the bi-4 tensor-border $\tilde{\mathbf{t}}$ of Fig. 6 g. Fig. 6 h shows $\tilde{\mathbf{t}}$ as the gray-underlaid layers of BB-coefficients of the bi-4 cap structure. While this multi-step re-approximation of the original expansions at the anchors is involved, the result is a formula that linearly maps the data in Fig. 6 b to Fig. 6 h, i.e. a linear map from N^1 to $\tilde{\mathbf{t}}$.

Next an auxiliary construction is applied symbolically to $\tilde{\mathbf{t}}$ to obtain an explicit formula for $\odot$ as a weighted sum of $\tilde{\mathbf{t}}$: we enforce G^1 continuity between sectors and compute the remaining BB-coefficients by minimizing – over all n output patches $g_i, i = 0, \ldots, n-1$ – the functional $\sum_{i=0}^{n-1} \mathcal{F}_k g_i$ where $\mathcal{F}_k g := \int_0^1 \int_0^1 \sum_{i+j=k,i,j\ge 0} \frac{k!}{i!j!} (\partial_s^i \partial_t^j g(s,t))^2 \, ds\, dt$. Unlike [29] we compute both $\mathcal{F}_4$ and $\mathcal{F}_5$ and then define $\odot$ as the average of the resulting two options of central points.

3.3. Determination of the improved face point $\mathbf{f}^+$ *for* $n > 4$

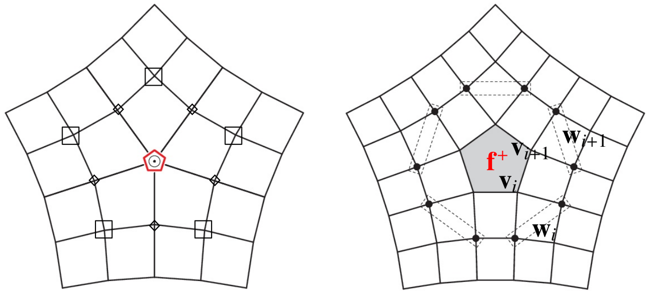

(a) from $\odot$ to ⬠

(b) re-grouped net N^0

Fig. 7: (a) Inverting the Catmull-Clark limit point formula yields the face point $\mathbf{f}^+$ = ⬠. (b) Grouping the nodes of the input net N^0 for the weights of the formula for $\mathbf{f}^+$.

The formula for the limit point $\odot$ of Catmull-Clark subdivision, see Fig. 7 a, is according to [27]:

$$\odot := \frac{n}{n+5}\,\text{⬠} + \frac{4}{n(n+5)}\sum_{i=0}^{n-1}\diamond_i + \frac{1}{n(n+5)}\sum_{i=0}^{n-1}\square_i. \tag{5}$$

Solving this equality for $\mathbf{f}^+$ = ⬠ yields

$$\mathbf{f}^+ = \frac{n+5}{n}\odot - \frac{4}{n^2}\sum_{i=0}^{n-1}\diamond_i - \frac{1}{n^2}\sum_{i=0}^{n-1}\square_i. \tag{6}$$

Computing $\mathbf{f}^+$ for valencies $n = 5, 6, 7, 8$, we observe that the weights of the vertices in the polyhedral net that are not direct neighbors of the multi-sided face amount to less that 1% in absolute value. We therefore minimize the footprint of the formula by setting them to 0. Next, let $\mathbf{w}_i$ be the average of direct neighbors of $\mathbf{v}_i$ that are not on the central face. By combinatorial symmetry, the weights corresponding to the n-sided face are all identical. We call this weight r_n. Then $\mathbf{f}^+$ is re-defined as

$$\mathbf{f}^+ := r_n \sum_{i=0}^{n-1} \mathbf{v}_i + \left(\frac{1}{n} - r_n\right) \sum_{i=0}^{n-1} \mathbf{w}_i. \tag{7}$$

For the exotic cases $n > 8$, we select the lowest degree rational interpolant $r(n) := \frac{a_0 + a_1 n}{1 + a_2 n + a_3 n^2}$, normalized so that the denominator constant is 1, to reproduce r_n for $n = 5, 6, 7, 8$. That is, we determine the coefficients a_i by enforcing $r(n) := r_n$ for $n = 5, \dots, 8$. With 5-digits accuracy

$$\begin{aligned} r_n &:= \frac{a_0 + a_1 n}{1 + a_2 n + a_3 n^2}, \text{ where} \\ a_0 &:= 2.64309,\ a_1 := -0.45291, \\ a_2 &:= 1.94025,\ a_3 := -0.36163. \end{aligned} \tag{8}$$

As hoped for, this r_n decreases monotonically with n, $r_n \to 0$ as $n \to \infty$, and $r_n > \frac{1}{n}$ for $n > 4$. We computed the weights for $n = 9, \dots 12$ the hard way, following Section 3.2 and this section. Remarkably, the resulting weights match the formula for r_n within a few percent! Setting $\mu_n := n r_n$ yields formula (2). Section 4 shows that the improved face rule, and the generalized edge rule $E^\star$, combined in *FEV**, provide refined nets that permit completion to high surface quality.

Determining a good choice of $\mathbf{f}^+$ is the key achievement of this paper.

3.4. Valence $n = 3$ and $n = 4$

As usual, the case $n = 3$ requires special consideration to obtain high quality surfaces. The computations of Section 3.2 and Section 3.3 (using the improved limit point rule in [4]) yield $r_3 \approx 0.235$. This results in too flat a vicinity of the central point, see Fig. 9 c. By contrast, the classic choice $r_3 := \frac{1}{3}$ yields an undesirable spike, see Fig. 9 d. Since numerous experiments show that $\frac{1}{4} < r_3 < \frac{1}{3}$ should hold, we set $r_3 := \frac{1}{2}(\frac{1}{4} + \frac{1}{3}) = \frac{7}{24}$. Fig. 9 e shows that this simple choice works well (and as well or better than values obtained by sophisticated experiments). Therefore $\mu_3 := 3r_3 = \frac{7}{8}$.

The value $r_4 := \frac{1}{4}$ coincides with regular refinement of uniform B-spline knot insertion.

4. Examples and Discussion

This section presents examples and discusses choices in the derivation of the algorithm. The examples include polyhedral nets with one multi-sided face, nets with T-junctions and nets with many and tightly-packed irregularities. To cover the multi-sided surface region, called *cap* hereafter, we examine the effect on four cap constructions: [1], [16], [4], [21]. [1] and [16] perform subdivision to the limit. [4] and [21] construct polynomial surfaces consisting of a finite number of pieces. [4] generates n patches of degree bi-5 (bi-4 if $n = 3$). [21] generates a short sequence of rapidly contracting bi-4 rings closed by a tiny bi-4 cap. We note that the new first step rule aims to reduce large scale artifacts and undue flatness in particular. We cannot expect a single refinement step to remedy all high-frequency artifacts of the capping algorithm.

4.1. Surfaces from a control net with central multi-sided face

The examples use a polyhedral net consisting of one multi-sided face surrounded by three layers of quadrilaterals, see Fig. 8 a such that all interior nodes are of valence 4. The polyhedral net defines one bi-3 ring (green in Fig. 8 b) that allows assessing the quality of the transition from a regular bi-3 surface to the area influenced by the refinement rules.

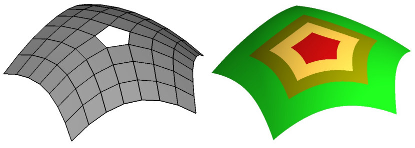

(a) polyhedral net, $n = 5$ (b) layout

(c) *FEV* + [4] (d) *FEV** + [4] (e) special + [4]

Fig. 8: Surfaces from convex $n = 5$ net.

The bronze and yellow bi-3 surface rings are defined by the once-refined net with the new face point f^+ critical to the construction of the yellow ring. The bi-5 cap is constructed according to [4]. Rule *FEV* widens the highlight lines,see Fig. 8 c, an indication of flatness, while *FEV** generates more uniform though not perfect highlight lines, Fig. 8 d. For this specific net, defining the weight of *FEV** by $\tilde{r}(n) := \gamma r(n) + (1-\gamma)\frac{1}{n}$, $\gamma := 0.8$, reduces oscillation further, see Fig. 8 e. But even such special case experimentation cannot fix high-frequency oscillations introduced at the transition to the surface cap.

For valence $n = 3$, Fig. 9 b shows the well-known pinched highlight lines when *FEV* is applied. Fig. 9 c vs. d motivates the special rule in Section 3.4 to avoid flatness when $n = 3$.

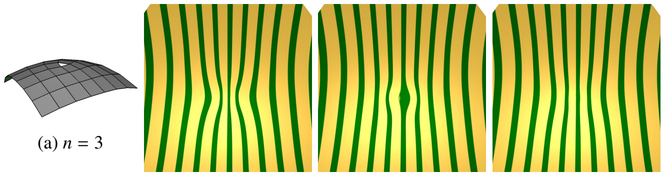

(a) $n = 3$ (b) *FEV*+[21] (c) as for $n > 4$ (d) *FEV**+[21]

Fig. 9: Input: (a) convex $n = 3$ net,

Fig. 10 juxtaposes *FEV* and *FEV** applied to a sequence of polyhedral nets resembling truncated cones. Such input is challenging for standard subdivision algorithms. Surfaces constructed by standard subdivision algorithms end up with an undesirably non-uniform highlight line distributions. The artifacts increase with n and are clearly visible for $n > 6$. The silhouettes of Fig. 10 b illustrate flatness caused by rule *FEV*. The highlight lines of the top view in Fig. 10 c confirm flatness by bulging at the center. Applying rule *FEV** remedies the flatness. However the subdivision rules of [16] result in oscillations of ever higher frequency, see Fig. 10 d . The highlight lines of Fig. 10 e are ‘tame’ by comparison, but still flawed: the hard problem of good shape for truncated cone input meshes requires not just an improved first step rule but also a globally shape sensitive surface construction. In any case, *FEV** yields better highlight line distributions.

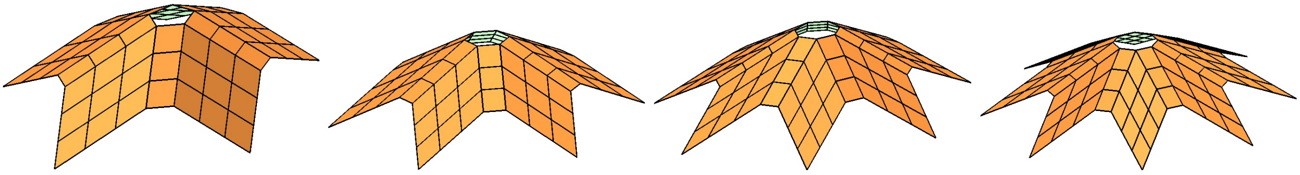

(a) . $n = 5$ $n = 6$ $n = 7$ $n = 8$

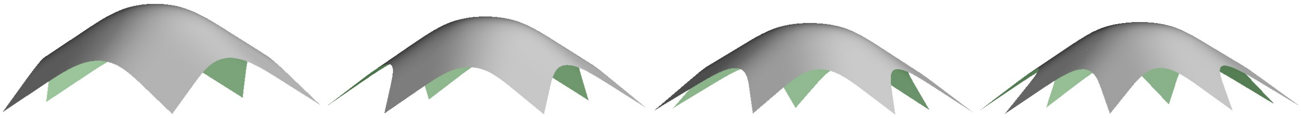

(b) side-view of *FEV* + [4]

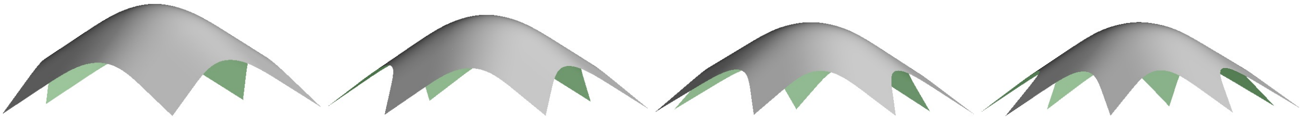

(c) side-view of $FEV^\star$ + [4]

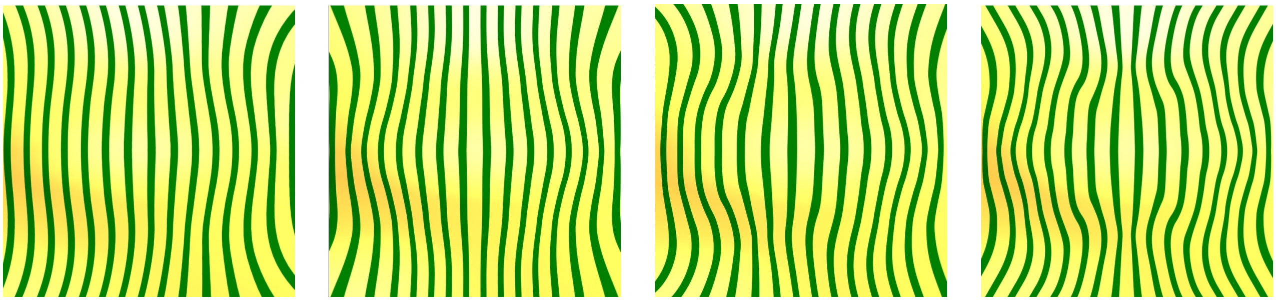

(d) top-view, highlight lines of *FEV* + [4]

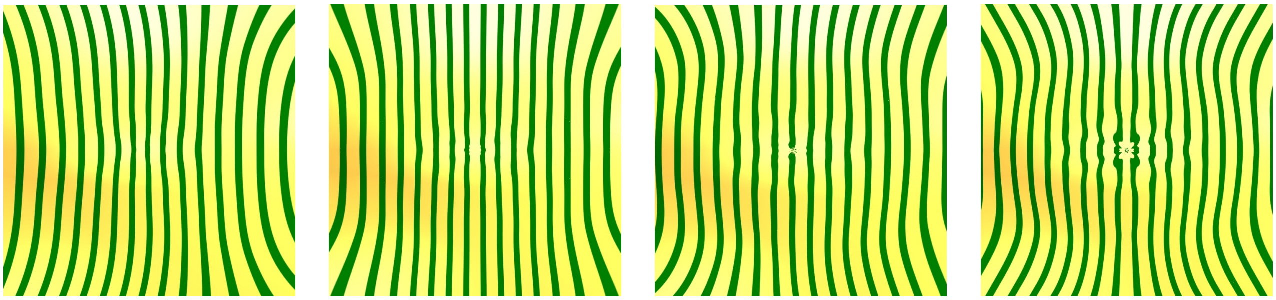

(e) top-view, highlight lines of $FEV^\star$ + [16]

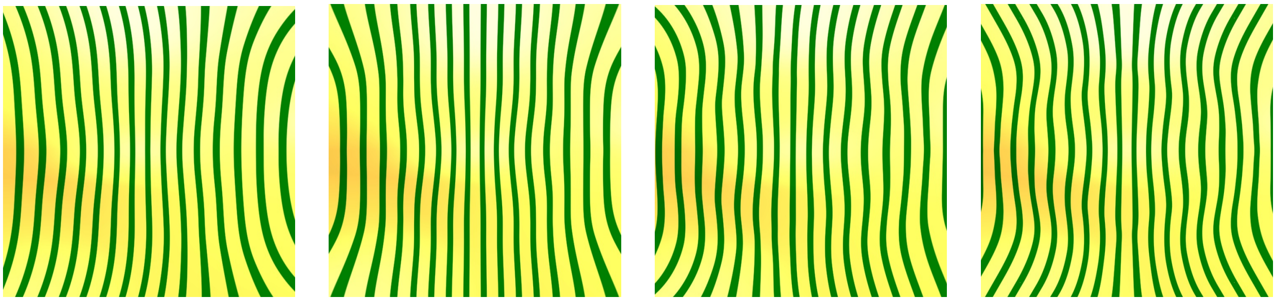

(f) top-view, highlight lines of $FEV^\star$ + [4]

Fig. 10: ‘Truncated cone’ input meshes. (a) a sequence of convex input nets for $n = 5, 6, 7, 8$. (b,c) side-view: the silhouette shows flatness when *FEV* is used. (c,d,e) top-view: increased oscillation of highlight lines with valence.

Fig. 11 c vs d shows the reduction in oscillation when $FEV^\star$ is chosen over FEV. Fig. 11 b vs d demonstrates the impact of the new *edge* rule in $FEV^\star$: the improved edge rule remedies the artifact pointed to by ↓. Row 3 again demonstrates a reduction in oscillation (see ↓) when FEV is replaced by $FEV^\star$. (When [21] is replaced by Catmull-Clark subdivision the oscillation turns into pinching highlight lines.) Row 4 illustrates reduction of flatness when FEV is replaced by $FEV^\star$.

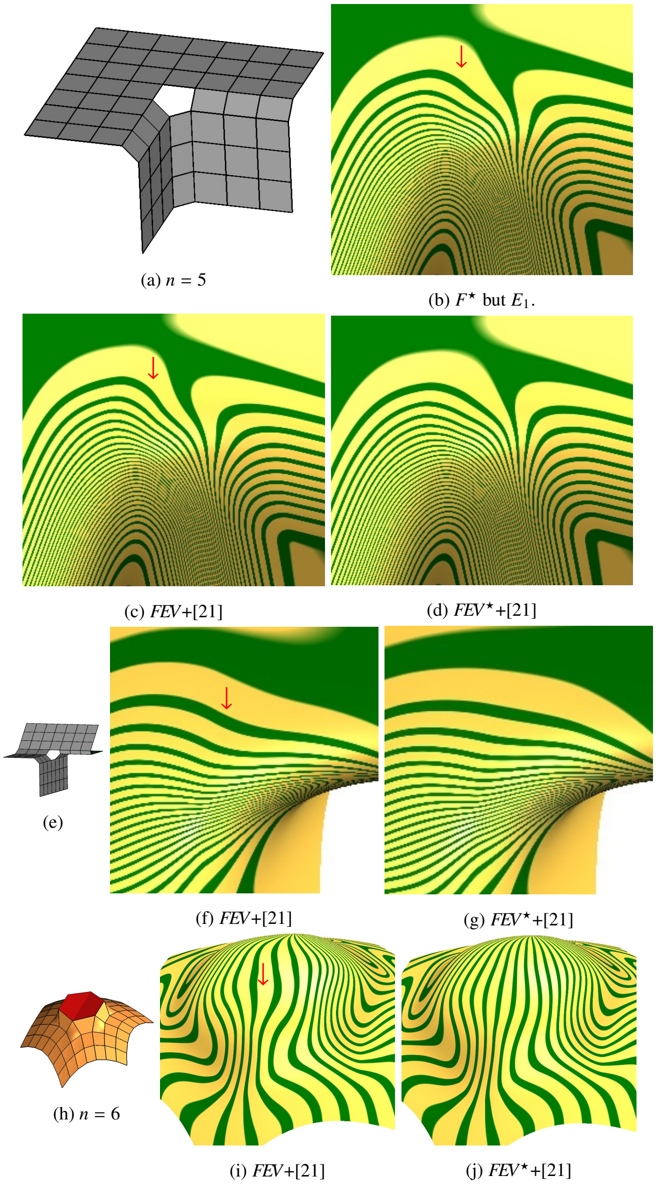
(a) $n = 5$
(b) $F^\star$ but E_1.
(c) FEV+[21]
(d) $FEV^\star$+[21]
(e)
(f) FEV+[21]
(g) $FEV^\star$+[21]
(h) $n = 6$
(i) FEV+[21]
(j) $FEV^\star$+[21]

Fig. 11: Input nets: (a) Two-beam $n = 5$, (e) Two-beam $n = 6$. (h) convex $n = 6$ net with extruded hexagonal face. The improved rule reduces oscillations.

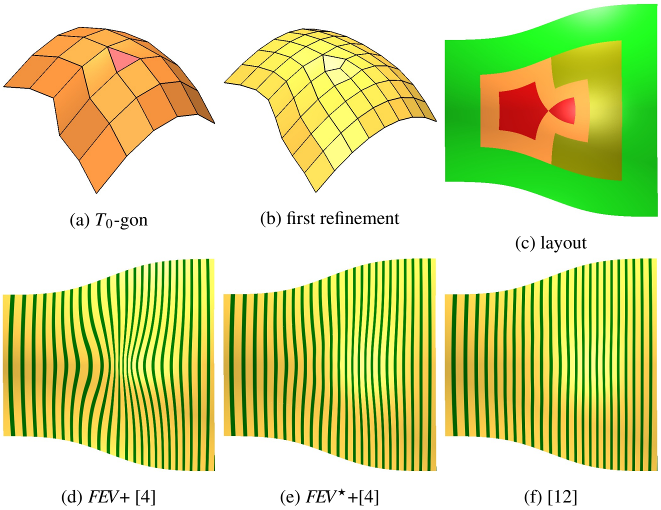
(a) T_0-gon
(b) first refinement
(c) layout
(d) FEV+ [4]
(e) $FEV^\star$+[4]
(f) [12]

Fig. 12: T_0-gon: (c) Layout: green bi-3 from input, bi-3 after 1st refinement, gold after 2nd, red multi-sided caps. While the surface (d) based on one FEV has strongly oscillating highlight lines, the naive use of the improved rule and [4] (e) comes remarkably close to the quality to the specialized construction [12] (f) for T-junctions.

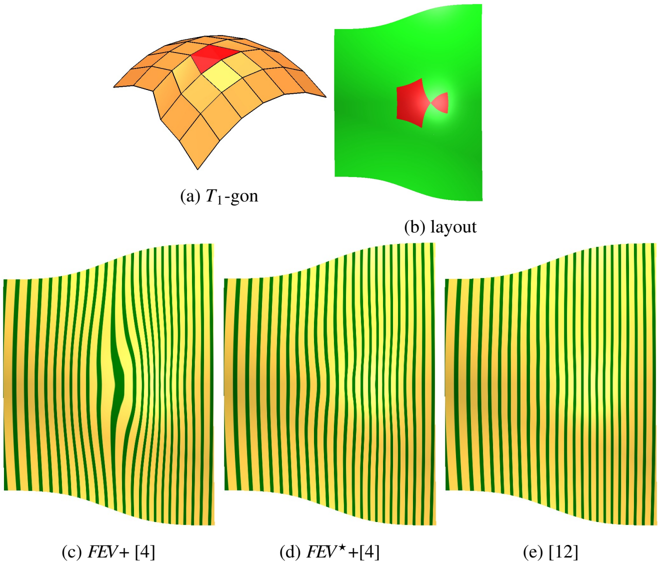
(a) T_1-gon
(b) layout
(c) FEV+ [4]
(d) $FEV^\star$+[4]
(e) [12]

Fig. 13: T_1-gon: (b) Layout: green bi-3 from input and first refinement, red multi-sided caps. While the surface (c) based on one FEV has strongly oscillating highlight lines, the naive use of the improved rule and [4] (d) comes remarkably close to the quality to the specialized construction [12] (e) for T-junctions.

4.2. Surfaces from nets with T-junctions

T-junctions allow a mesh to transition from fine to coarse. Polyhedral modelers use T-junctions to reduce (or increase) the number of quad strips in one direction. We will see that for T-junctions, a specialized construction does better than applying the direction-agnostic improved rule plus a generic surface construction. This is unsurprising. What is surprising is how well the improved rule does in comparison to the specialized algorithm [12].

A T_0-gon is a triangle surrounded by quads and such that one vertex has 5 neighbors, while the other two have 4, see Fig. 12 a.

A T_1-gon is nominally a pentagon: 4 of its vertices have regular valence 4 while one, the fifth is a vertex of valence 3, the T-junction, see Fig. 13 a. Due to the T-junction the pentagon can be interpreted as one large quad meeting two smaller quads across one edge split by the T-junction. Also, T-gons are generated by some quad-dominant re-meshing algorithms [8, 9]. To obtain a pure quad-mesh, the default approach is to apply one Catmull-Clark step. However [30] demonstrated that this step negatively influence the shape of subsequent surface constructions that use the quad-mesh as a generalized control net. The new rule can serve as the 'poor man's' easily-implemented alternative to refinement or specialized treatment of T-junctions by algorithms such as [10, 11, 12].

Fig. 12 and Fig. 13 illustrate that rule *FEV** improves over *FEV*, although the highlight line distribution is not as good as for construction specialized to T-junctions such as [12]. Note, however, that [12] demands sufficient separation between T-gons, whereas the improved rule can be applied to any configuration and the resulting refined net can still yield surfaces of good quality. For both T_0- and T_1-gons the once-refined net contains a face with unseparated special nodes, namely a vertex of valence $n = 3$ and one of valence $n = 5$. The required second refinement step yields the regular bi-3 patches shown in bronze and orange in Fig. 12 .

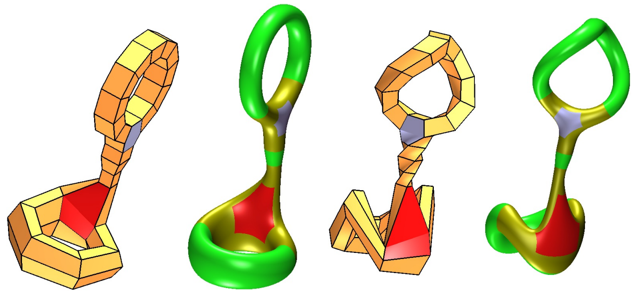
(a) Genus 2 net and layout (b) Twisted

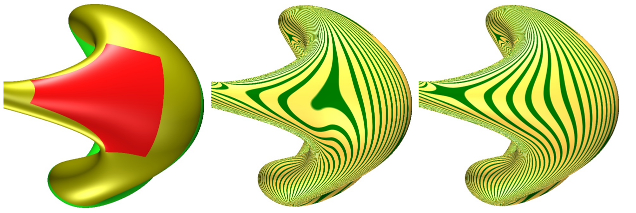
(c) Magnified base (d) *FEV*+ [4] (e) *FEV**+[4]

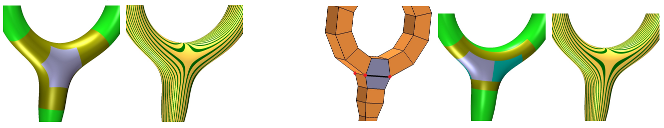
(f) Zoom on neck (g) Re-mesh using 5-valent nodes

Fig. 14: Surfaces of genus 2 from meshes with regular vertices and with four 6-sided faces besides quads.

4.3. *Surfaces from meshes with many and tightly-packed irregularities*

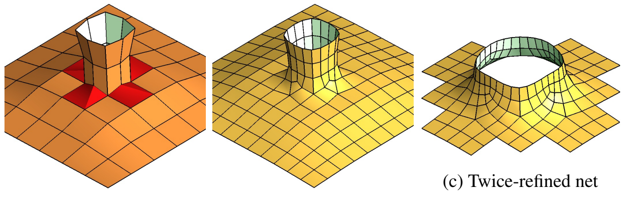
(a) polyhedral net (b) quad net Q (c) Twice-refined net

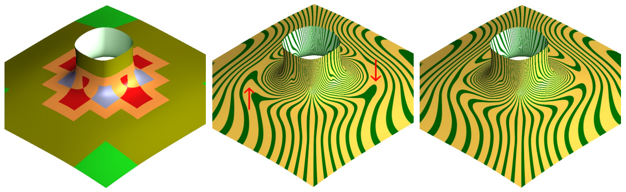
(d) layout (e) *FEV*+ [4] (f) *FEV**+[4]

Fig. 15: Control nets with T-joints. (a) polyhedral net: four T_1-gons pairwise share corner vertices of valence 5. (b) once-refined quad net Q. (c) Second refinement. (d) surface layout of the surface. Only the green bi-3 patches are directly from the regular parts of the polyhedral net. The green-bronze bi-3 patches are from the quad net Q. The gold bi-3 patches and the multi-sided caps are generated from the second refinement net (c). (e) The flatness induced by the *FEV* shows in the expanded highlight lines compared to (f).

Fig. 14 validates once again the advantages of the improved rule for a more complex design. The bottom row serves to compare the outcome when modeling with multi-sided faces Fig. 14 f *vs* with multi-valent nodes Fig. 14 g: there is no visible difference in the resulting surface quality but the multi-sided face design require less effort.

Inspired by a challenging example of 'dyadic subdivision' [11], Fig. 15 starts with tightly packed T-junctions such that some corner vertices have valence $n = 5$. Since the elongated highlight lines in (e) compared to (f) indicate relative flatness, there is a clear improvement in (f) over (e), i.e. *FEV** over *FEV*.

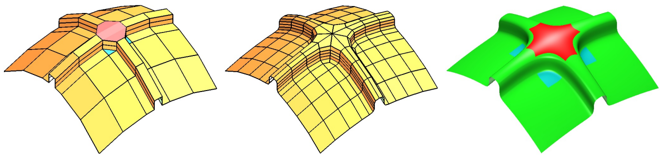
(a) mesh (b) *FEV** refinement (c) layout

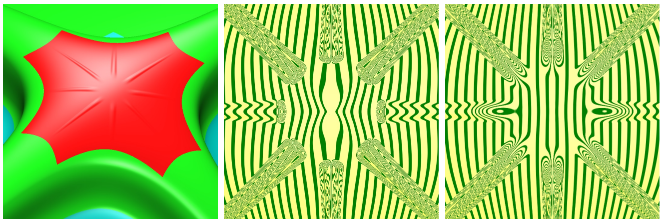
(d) detailed editing (e) 1new + [1] (f) 1new + [21]

Fig. 16: Detailed design. (a) input mesh with one 8-sided and four 3-sided faces; (b) refinement; (d,e,f) zoom into the 8-sided area with added ridges.

Fig. 16 demonstrates the importance of the cap algorithm for a complex design that combines one 8-sided and four 3-sided faces, and adds ridges, see Fig. 16 d. A cap using [1] to model the ridges results in pinched highlight lines near the extraordinary point Fig. 16 e. A cap leveraging the hierarchical structure of the refinable degree bi-4 surface cap [21] to model ridges results in a far better highlight line distribution near the extraodinary point, see Fig. 16 f. This illustrates once more that while a single, first step cannot fix the known deficiencies, here a pinching of highlight lines of a subsequent subdivision algorithm, the new step allows for a well-shaped surface completion by high-end constructions.

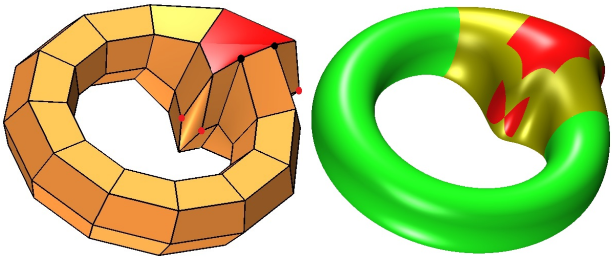
(a) Input net (b) layout

Fig. 17: Input net does not admit a T-spline surface: (a) two 6-sided faces (red), each containing two T-junctions, of unusual valence 4 (marked as •); two quads each have two vertices of valence 3 (marked as •). (b) original bi-3 patches, bi-3 patches due to refinement, multi-sided construction.

The T-joints in the ring configuration in Fig. 17 breaks T-spline constructions [10]: edges to the left of the left • and to the right of the right • (but not between bullets) must have zero knot intervals. Refinement would therefore create a sequence of zero-length intervals, i.e. discontinuity in the parameterization. Again the *improvement* due to rule $\mathit{FEV}^\star$ over *FEV* is evident, regardless of whether the surface is capped with Catmull-Clark subdivision to the limit, Fig. 18 b, with the subdivision method of [16], Fig. 18 c, or with the construction of [4], Fig. 18 d.

4.4. *Boundary rules*

Multi-sided faces on the boundary are treated via the default approach for all subdivision algorithms: a phantom boundary layer of quads is added. A specific choice of phantom layer in terms of the original mesh nodes then yields 'new' boundary rules. A particularly simple choice is to make the phantom layer identical to the current boundary, i.e. adding zero-area quads, see blue boundaries in Fig. 19 a and Fig. 20 a. This choice places the new face point closer to the pentagon center of the (F) rule than for configuration Fig. 8 . Still the flatness in Fig. 19 c and Fig. 20 c evident from the wider spread of the highlight lines for the *FEV* step is essentially reduced.

5. Conclusion

The new first-step refinement rules $F^\star$ and $E^\star$ for multi-sided faces improve the chances for good outcomes when using the refined mesh to construct multi-sided surface caps. The new rules remedy the visible first-step shape artifacts of the classical Catmull-Clark step – that defeat even high-quality constructions. The rule $\mathit{FEV}^\star$ provides a 'general purpose' improvement at a modest cost: the new face rule has a moderately increased footprint and remains simple in that it is characterized by just one scalar weight for each n.

Acknowledgements. This work was supported in part by DARPA HR00111720031 and NIH R01 EB018625.

References

[1] E. Catmull, J. Clark, Recursively generated B-spline surfaces on arbitrary topological meshes, Computer-Aided Design 10 (1978) 350–355.

[2] K.-P. Beier, Y. Chen, Highlight-line algorithm for realtime surface-quality assessment, Comp-Aid Design 26 (4) (1994) 268–277.

[3] J. Peters, U. Reif, Subdivision Surfaces, Vol. 3 of Geometry and Computing, Springer-Verlag, New York, 2008.

[4] K. Karčiauskas, J. Peters, Improved shape for multi-surface blends, Graphical Models 8 (2015) 87–98.

[5] P. Alliez, D. Cohen-Steiner, O. Devillers, B. Lévy, M. Desbrun, Anisotropic polygonal remeshing, ACM Tr Graph 22(3) (2003) 485–493.

[6] M. Marinov, L. Kobbelt, Direct anisotropic quad-dominant remeshing, in: Proceedings of the Computer Graphics and Applications, 12th Pacific Conference, PG '04, IEEE Computer Society, Washington, DC, USA, 2004, pp. 207–216.

[7] Y.-K. Lai, L. Kobbelt, S.-M. Hu, An incremental approach to feature aligned quad dominant remeshing, in: E. Haines, M. McGuire (Eds.), Symp Solid & Phys Modeling, ACM, 2008, pp. 137–145.

[8] W. Jakob, M. Tarini, D. Panozzo, O. Sorkine-Hornung, Instant field-aligned meshes, ACM Trans. Graph 34 (6) (2015) 189.

[9] N. Schertler, M. Tarini, W. Jakob, M. Kazhdan, S. Gumhold, D. Panozzo, Field-aligned online surface reconstruction, ACM Trans. Graph 36 (4) (2017) 77:1–77:13.

[10] T. W. Sederberg, J. Zheng, A. Bakenov, A. Nasri, T-splines and T-NURCCs, in: J. Hodgins, J. C. Hart (Eds.), Proc ACM SIGGRAPH, Vol. 22(3) of ACM Tr Graph, 2003, pp. 477–484.

[11] D. Kovacs, J. Bisceglio, D. Zorin, Dyadic T-mesh subdivision, ACM Trans. Graph. 34 (4) (2015) 143:1–143:12.

[12] K. Karčiauskas, J. Peters, High quality refinable G-splines for locally quad-dominant meshes with T-gons, Computer Graphics Forum 38 (5) (2019) 151–161.

[13] K. Karciauskas, J. Peters, U. Reif, Shape characterization of subdivision surfaces – case studies, Computer-Aided Geometric Design 21 (6) (2004) 601–614.

[14] K. Karčiauskas, J. Peters, Concentric tesselation maps and curvature continuous guided surfaces, Computer Aided Geometric Design 24 (2) (2007) 99–111.

[15] T. J. Cashman, U. H. Augsdörfer, N. A. Dodgson, M. A. Sabin, NURBS with extraordinary points: high-degree, non-uniform, rational subdivision schemes, ACM Tr Graph 28 (3) (2009) 46:1–46:9.

[16] Y. Ma, W. Ma, Subdivision schemes with optimal bounded curvature near extraordinary vertices, Computer Graphics Forum 37 (7) (2018) 455–467.

[17] X. Li, G. Finnigan, T. Sederberg, G^1 non-uniform Catmull-Clark surfaces, ACM Transactions on Graphics 35 (2016) 1–8.

[18] M. Sabin, L. Barthe, Artifacts in recursive subdivision surfaces, in: A. Cohen, J. L. Merrien, L. L. Schumake (Eds.), Curve and Surface Fitting, Nashboro Press, http://www.nashboro.com, 2003, pp. 353–362.
URL http://www.irit.fr/~Loic.Barthe/publications.php

[19] U. H. Augsdörfer, N. A. Dodgson, M. A. Sabin, Artifact analysis on B-splines, box-splines and other surfaces defined by quadrilateral polyhedra, Comp Aid Geom Design 28 (3) (2011) 177–197.

[20] C. T. Loop, S. Schaefer, G^2 tensor product splines over extraordinary vertices, Comput. Graph. Forum 27 (5) (2008) 1373–1382.

[21] K. Karčiauskas, J. Peters, Curvature-bounded guided subdivision: biquartics vs bicubics, Computer Aided Design (2019) 1–11.

[22] T. Várady, P. Salvi, A. P. Rockwood, Transfinite surface interpolation with interior control, Graph. Model 74 (6) (2012) 311–320.

[23] P. Salvi, T. Várady, A. P. Rockwood, Ribbon-based transfinite surfaces, Comput. Aided Geom. Des 31 (9) (2014) 613–630.

[24] G. J. Hettinga, J. Kosinka, A multisided C^2 B-spline patch over extraordinary vertices in quadrilateral meshes, Comput. Aided Des 127 (2020) 102855.

[25] G. J. Hettinga, J. Kosinka, Multisided B-spline Patches Over Extraordinary Regions, in: S. Biasotti, R. Pintus, S. Berretti (Eds.), Smart Tools and Apps for Graphics - Eurographics Italian Chapter Conference, The Eurographics Association, 2020.

[26] G. J. Hettinga, J. Kosinka, Multisided generalisations of Gregory patches, Computer Aided Geometric Design 62 (2018) 166–180.

[27] M. Halstead, M. Kass, T. DeRose, Efficient, fair interpolation using catmull-clark surfaces (1993) 35–44.

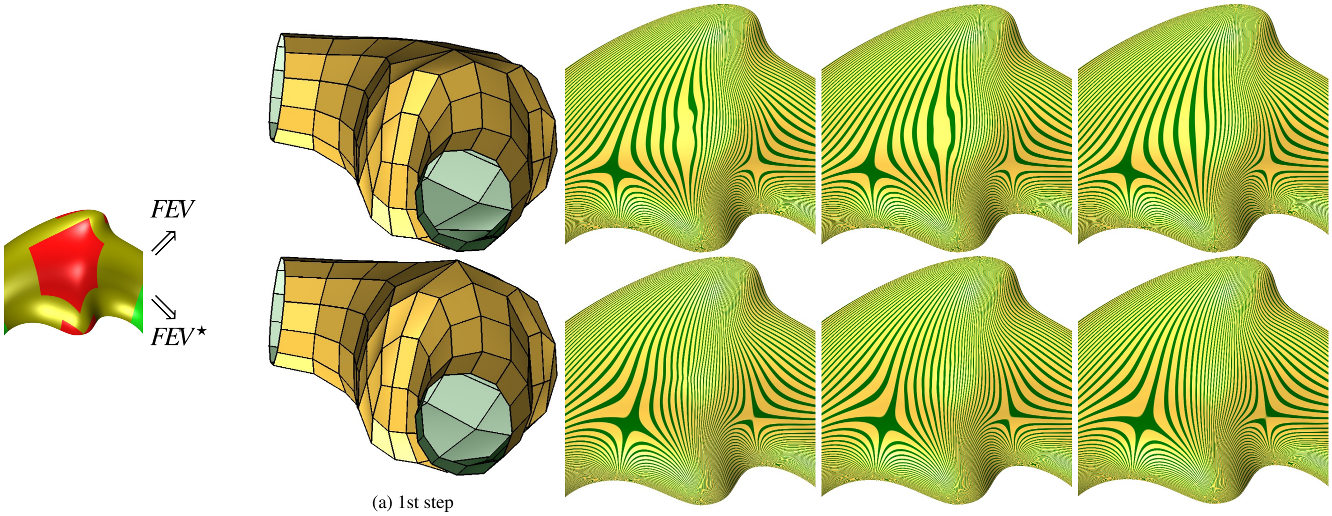

(a) 1st step

(b) Catmull-Clark (c) [16] (d) [4]

Fig. 18: Impact on the vicinity of 6-sided faces, choosing as the first refinement step either (*top*) *FEV* or (*bottom*) *FEV**.

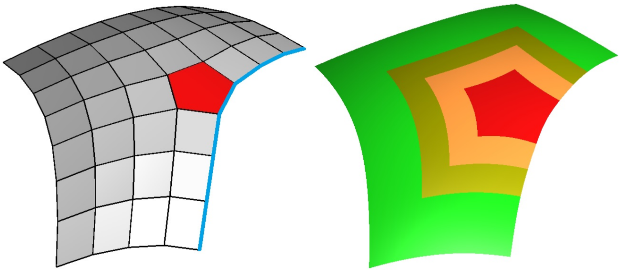

(a) polyhedral net, $n = 5$ (b) layout

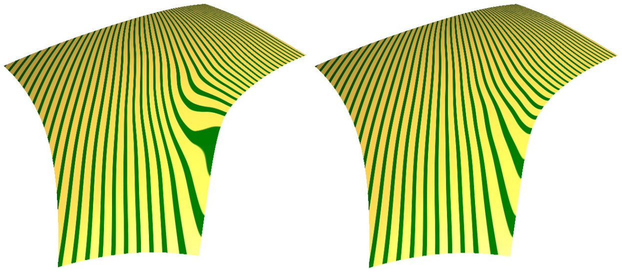

(c) *FEV*+[21] (d) *FEV**+[21]

Fig. 19: Multi-sided boundary face managed with a zero-width phantom layer (blue).

[28] G. Farin, Curves and Surfaces for Computer Aided Geometric Design: A Practical Guide, Academic Press, 1988.
[29] K. Karčiauskas, J. Peters, Least degree G^1-refinable multi-sided surfaces suitable for inclusion into C^1 bi-2 splines, Computer-Aided Design 130 (2021) 1–12.
[30] K. Karčiauskas, D. Panozzo, J. Peters, T-junctions in spline surfaces, ACM Tr on Graphics 36 (5) (2017) 170:1–9.

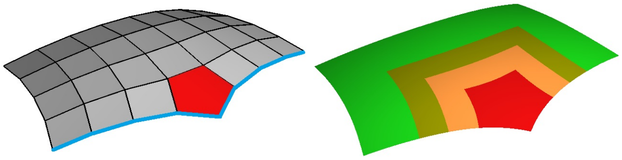

(a) polyhedral net, $n = 5$ (b) layout

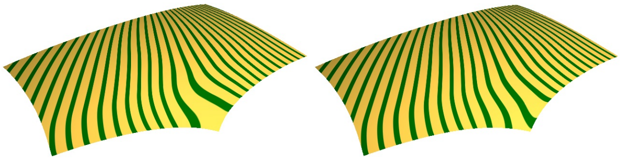

(c) *FEV*+[21] (d) *FEV**+[21]

Fig. 20: Multi-sided boundary face with exposed corner managed with a zero-width phantom layer (blue).